RSC Advances

ROYAL SOCIETY OF CHEMISTRY

www.rsc.org/advances

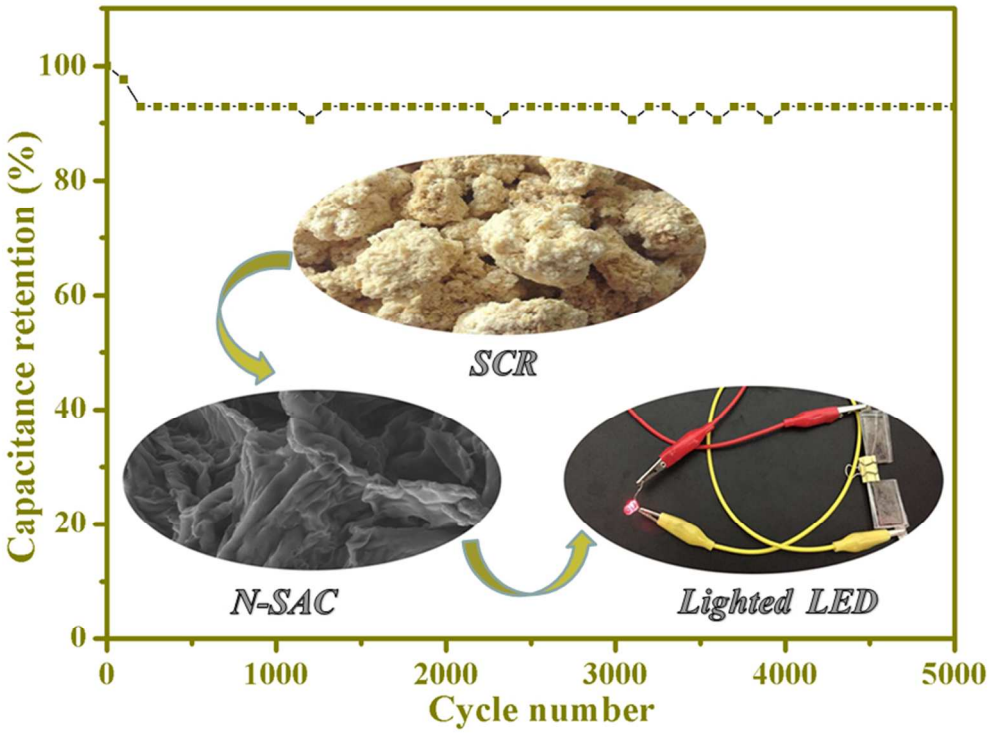

239x175mm (96 x 96 DPI)

Nitrogen-doped Porous Carbon Obtained via One-step Carbonizing Biowaste Soybean Curd Residue for Supercapacitor Application

Guofu Ma[a*], Feitian Ran[a], Hui Peng[a], Kanjun Sun[b], Zhiguo Zhang[a], Qian Yang[a], Ziqiang Lei[a]*

[a]*Key Laboratory of Eco-Environment-Related Polymer Materials of Ministry of Education, Key Laboratory of Polymer Materials of Gansu Province, College of Chemistry and Chemical Engineering, Northwest Normal University, Lanzhou 730070, China.*

[b]*College of Chemistry and Environmental Science, Lanzhou City University, Lanzhou 730070, China.*

E-mail: magf@nwnu.edu.cn, leizq@nwnu.edu.cn

ABSTRACT: In this work, we present a facile approach to prepare nitrogen-doped porous carbon materials via one-step carbonizing biowaste soybean curd residue (SCR) as the biomass carbon precursor. The morphology, structure and textural properties of the carbon materials are investigated by field emission scanning electron microscopy, transmission electron microscopy, N_2 sorption isotherms, and X-ray photoelectron spectroscopy, respectively. The SCR carbonized at 700 ^{o}C exhibits high charge storage capacity with a specific capacitance of 215 F g^{-1} at a current density of 0.5 A g^{-1} and good stability over 5000 cycles. Moreover, the assembled symmetric supercapacitor device possesses a energy density of 9.95 Wh kg^{-1} at a power density of 236 W Kg^{-1}, which is higher than that of commercially available supercapacitors. The high supercapacitor performance of the porous carbon can be due to the high surface area and effective nitrogen-doping, indicating it can be a great potential for supercapacitors.

KEYWORDS: Biowaste; Soybean curd residue; Nitrogen-doping; Supercapacitors

1. Introduction

Efficient energy production and storage in an eco-friendly and sustainable way has become a global objective.[1] Electrochemical technology as an effective electrical energy storage strategy has attracted immense attention, and many rechargeable devices have been developed.[2] Among these devices, supercapacitors play an important role for energy storage due to the advantages such as the high power capability, good coulombic reversibility (98% or higher), excellent cyclability (>100,000 cycles) and environmentally friendly property.[3,4] Based on the charge-storage mechanism, supercapacitors can be divided into two main classes: electrical double-layer capacitor (EDLC) and pseudocapacitor.

Carbons materials have been widely used as typical electrode materials of EDLCs due to their high specific surface area, excellent electronic conductivity, high chemical stability, low cost and long cycle life.[5-8] However, compared with most pseudocapacitor electrode materials such as metal oxides and conductive polymers, carbon-based electrode materials offer lower specific capacitance and energy density in supercapacitor applications.[9] Therefore, various attempts have been made to improve the electrochemical performance of carbons materials for its further applications. One effective approach is to introduce heteroatoms and functional groups into carbocyclic rings, which has attracted considerable attention for energy storage devices.[10] The incorporation of nitrogen, for example, was found to possess improved electrical conductivity compared to their pure counterparts.[11] Moreover, the nitrogen-containing functional groups can induce pseudocapacitive effects and improve the wettability of carbon materials to electrolyte solution.[12] What's more, nitrogen doping can increase the electronic conductivity of carbon materials significantly.[13] However, plenty of nitrogen-doped carbon materials have been acquired

by post-treatment, such as treating with ammonia gas or undergoing a carbonization of the nitrogen-enriched precursor, which always involves hazardous working conditions or time-consuming synthetic processes.[14] Meanwhile, a large volume of waste water was generated in the process of preparation of carbon materials via the use of the activation agent, which caused serious environmental pollution. Consequently, one of the promising but challenged direction is to prepare cost-effective and sustainable porous carbon materials with high surface area, low pore volume, hierarchical porous structure and tailored heteroatom functionalities derived from environmental friendly renewable biomass.[15,16]

Recently, considering the demand for sustainable eco-friendly resources and process, more and more attention has been focused on utilizing sustainable biomass wastes precursors to synthesize the porous carbons as electrode material for supercapacitor application.[17] Due to natural abundance and low-cost, several porous carbon materials are derived from carbonizing biomass waste as precursors, such as human hair,[15] coffee grounds,[18] cow dung[19] and corncob residue.[17] They all exhibit favorable electrochemical capacitance performances. Meanwhile, the development and utilization of biomass waste materials could contribute to explore novel materials for long-term sustainable energy storage, enhance cost competitiveness in energy supply markets, reduce environmental impacts and meet the urgent need for green and sustainable development strategies.[15]

Soybean curd residue (SCR), the by-product of soybean curd, soymilk and other soybean products processing, is a cheap and available resource in Asian countries. Currently, SCR is just discharged as agro-industrial waste because it is highly susceptible to putrefaction, most of the SCR was incinerated artificially and caused severe environmental pollution, except a little used as

feed stuff.[20-23] Despite their abundance, the investigations on how to transform SCR into valuable products are still very limited, and find a green and simple strategy to turn the residue into high value materials is very meaningful. Especially, SCR is a loose material consisting of protein, oil, dietary fiber, minerals, along with unspecified monosaccharides and oligosaccharides.[20] Therefore, the SCR should be a promising nitrogen-enriched precursor for the preparation of nitrogen-doped porous carbons.

In the present work, SCR is used as a nitrogen-enriched precursor to prepare nitrogen-doped porous carbon via one-step carbonizing method. The electrochemical performance of porous carbons with different nitrogen contents as electrode material of supercapacitors were studied in 2 M KOH aqueous electrolyte, and their relationships with morphology, structures, specific surface area and electrochemical characteristics of the carbon samples are also discussed in detail.

2. Experimental

2.1. Materials

Fresh SCR (moisture content 80%) was obtained from local bean products processing factory (Lanzhou, China), and the residual water was removed by drying at 60 ^{o}C. In this study, the SCR with a particle size of 600 μm was used and all SCR was obtained from the same batch in the manufacturing process. Potassium hydroxide (KOH, Sinopharm Chemical Reagent Co., Ltd., China, AR) was used as received without any further purification. Distilled water was used to prepare solutions and wash samples.

2.2 Preparation of nitrogen-doped porous carbon

The nitrogen-doped porous carbons were prepared from SCR as follows: the SCR fine powder was first washed with deionized water to remove dust and dried at 100°C for 24 h. Then 5 g of

SCR powder was placed in a porcelain boat and carbonized at 600, 700, 800, and 900 ^{o}C in a tube furnace (OTL 1200, Nanjing NanDa Instrument Co., Ltd., China) at a heating rate of 5°C min^{-1} under N_2 environment for 2 h. After cooled to room temperature, the obtained carbide samples were treated with HCl solution (2 mol L^{-1}) under stirring for 4 h to remove the inorganic salts and other impurities. Finally, the carbon samples were washed with distilled water until the pH value reached 7 and dried at 60 ^{o}C in ambient for 24 h. Herein, we refer the SCR powder and samples with the carbonize treatment as N-SAC600, N-SAC700, N-SAC800 and N-SAC900, respectively.

2.3 Characterization and electrochemical measurement

The morphologies of the obtained porous carbons were characterized by field emission scanning electron microscopy (FE-SEM, Ultra Plus, Carl Zeiss, German). Transmission electron microscopy (TEM) images were obtained using a JEM-1200EX microscope operating at 200 kV. The crystallographic information of the carbons was investigated by powder X-ray diffraction (XRD, D/Max-2400, Rigaku, Japan) diffractometer with Cu Kα radiation (k =1.5418 Å) at 40 kV, 100 mA. The 2θ measure range was from 5 to 80°. The Brunauer-Emmett-Teller surface areas (S_{BET}) of the obtained porous carbons were analyzed by using nitrogen adsorption in a Micromeritics ASAP 2020 nitrogen adsorption apparatus (U.S.A.). All samples were degassed at 200 ^{o}C prior to nitrogen adsorption measurements. The pore size distribution plots were recorded from the desorption branch of the isotherms based on the Barrett-Joyner-Halenda (BJH) model. Raman spectra were recorded with an inVia Raman spectrometer (Renishaw) with an Argon ion laser (λ= 514 nm). The element contents were measured by an Elementar CHNS analyzer model Vario EL III (Vario EL, Elementar Analyser systeme GmbH, Hanau, Germany). X-ray photoelectron spectroscopy (XPS) measurement was performed on an Escalab 210 system

(Germany) using a monochromatic Al Kα radiation source (ThermoVG Scientific).

2.4 Three-electrode system

In a three-electrode system, 5 mm diameter glassy carbon electrode, carbon rod and Hg/HgO electrodes serves as working electrode, counter electrode and reference electrodes, respectively. The working electrodes were fabricated similar to our previous reported literature [24]. Typically, 4 mg of active material (N-SACs) was ultrasonically dispersed in 0.4 mL of 0.25 wt% Nafion (DuPont, USA) ethanol solution. The homogenized suspension of 8 μL was dropped onto the surface of glassy carbon electrode using a pipette gun and dried at room temperature. The three-electrode system was test in 2 mol L^{-1} KOH aqueous solutions.

2.5 Two-electrode cell fabrication

The capacitive performance of N-SAC700 was further investigated using a two-electrode testing device. The working electrodes were typically fabricated by mixing the porous carbon as the active material (80 wt%), commercial carbon black (acetylene black, 10 wt%) and polymer binder (polyvinylidene fluoride, PVDF, 10 wt%) in N-methyl-2-pyrrolidone (NMP) solution until form homogeneous slurry. The slurry was coated on nickel foam current collectors and the electrodes were dried at 100 ^{o}C for 12 h in an oven, and then the premade electrodes were weighted and pressed into sheets under a pressure of 15 MPa. Each working electrode contained about 4 mg of active materials and had a geometric surface area of about circular 1 cm^2. Two electrodes with identical or very close weight were selected for the measurement.

Two as-prepared N-SAC700 electrodes fitted with the separator (filter paper) and electrolyte solution were symmetrically assembled into sandwich-type cells construction (electrode/separator/electrode). Before assembling the supercapacitor configuration, N-SAC700

electrodes and separator were immersed in 0.5 mol L^{-1} Na_2SO_4 electrolyte for 12 h to make aqueous electrolyte solutions homogeneously diffuse into the N-SAC700 electrode.

2.6 Electrochemical evaluation

The electrochemical properties of the samples were evaluated by cyclic voltammetry (CV) and galvanostatic charge/discharge in three-electrode and two-electrode system using a CHI660D electrochemical workstation. The cycle-life stability was performed using cycling testing equipment (CT2001A, Wuhan Land Electronic Co. Ltd., China). Electrochemical impedance spectroscopy (EIS) measurements were performed with the Autolab PGSTAT 128N equipped (Eco-chemie, Netherland) with FRA module, the frequency ranging from 10 mHz to 100 kHz and an impedance amplitude of ±5 mV at open circuit potential.

The gravimetric capacitance can be calculated from the charge/discharge curves of three-electrode system according to the equation of $C_g=I\Delta t/(m\Delta V)$, While, for the two-electrode cells, it was calculated by the equation of $C^*_g=I\Delta t/(m\Delta V)$, where I (A) is the constant discharging current, Δt (s) is the discharge time, ΔV (V) is the voltage window, m (g) is the mass of active materials loaded in the working (For the two-electrode cells, m is the total mass of active materials on the two electrodes of the supercapacitor cell).

Energy density and power density for a supercapacitor cell were calculated using equation: $E=1/2CV^2$, $P=E/t$, where C (F g^{-1}) represents the gravimetric capacitance of supercapacitor cell, V (V) refers to the voltage change within the discharge time Δt (s), E is the energy density (Wh kg^{-1}) and P is the power density (W kg^{-1}).

3. Results and discussions

3.1 The morphologies and structures of nitrogen-doped porous carbon samples

Scheme 1 shows the schematic drawing of preparation process of N-SACs from biomass waste SCR and the application of N-SAC700 as supercapacitor to light the light-emitting diode (LED). By one-step converting waste SCR to nitrogen-doped porous carbon, we can utilize waste materials to prepare novel electrode materials, which not only can develop the further convert waste materials to a long-term sustainable energy storage device (supercapacitor), but also reduce the environmental pollution.

The sample structural characters are seriously affected by the carbonization temperature. Figure 1 presents the FE-SEM images for the obtained porous carbon materials from different carbonization temperatures. It can be seen that the N-SAC600 exhibits a rough surface and no obvious porous morphology (Figure 1a). However, for the surface morphology of N-SAC700, it has many obvious wrinkles and significant pores with different pore sizes (Figure 1b). Similarly, when the carbonization temperature continues to increase, the wrinkled structure was destroyed. Precisely, the N-SAC800 (Figure 1c) and N-SAC900 (Figure 1d) have porous surfaces with integrated pores and more mesoporous developed on the surface of the carbons and even interconnected with each other. The TEM images (Figure 2) further reveal the porous structure of N-SAC700 with the pore sizes ranges from a few dozen nanometers to a micrometer. All of these phenomenons are probably caused by the release of residual gases during the carbonization process at high temperature. Those results demonstrate that the morphologies and structures of carbons could be improved at suitable carbonization temperature. In addition, the micro/mespores and interconnections structure could provide a favorable path for the electrolyte ions such as KOH and Na_2SO_4 to transport and penetrate, which indicates that the N-SACs could be promising supercapacitor electrode materials.[25]

The graphitic property of the N-SAC700 samples is investigated by wide-angle XRD patterns and Raman spectra. The XRD pattern of N-SAC700 is given in Figure 3a. Two typical diffraction peaks are observed at around 2θ = 21.7 and 43.1°, which belong to diffraction of the (002) and (100) planes of the hexagonal graphitic carbon, respectively. This indicates that the N-SAC700 is the turbostratic disordered carbon with low crystallinity between graphite and amorphous carbon.[19,26] In addition, the value of d_{002} is about 0.409 nm, larger than that of graphite (0.335 nm), implying a random combination of graphitic and turbostratic stacking.[27] The supporting evidence comes from Raman spectra analysis, and the typical Raman spectra of the obtained N-SAC700 sample is shown in Figure 3b. Two prominent peaks at about 1335 and 1596 cm^{-1} represent the D band and the G band, respectively, which are characteristic Raman peaks for carbon materials. The D-band is associated with the vibrations of carbon atoms with dangling bonds in plane terminations of the disordered graphite from the defects and disorders of structures in carbon materials, while G-band is attributed to the vibration of sp^2 hybridized carbon atoms in a 2D hexagonal lattice. Moreover, the intensity ratio of D-band to G-band (I_D/I_G) depends on the type of graphitic materials and reflects the graphitization degree.[28] From the Raman spectra of N-SAC700, it can be seen that the D-band peak is slightly weaker than the G-band peak and their intensity ratio (I_D/I_G) is about 0.97, indicating the formation of long-range graphitized carbon with a relatively small number of structural defects.

To further investigate the detailed textural and porosity characteristics of the obtained carbon materials under different carbonization temperature, nitrogen adsorption-desorption isotherm measurements were performed and the results are depicted in Figure 4a. The corresponding main textural parameters of N-SACs are summarized in Table 1. It can be seen that the porosity of the

N-SACs is significantly influenced by the activation temperatures. The N-SAC600 exhibits very low porosity with surface area of 9.78 $m^2 g^{-1}$ and pore volume of 0.016 $cm^3 g^{-1}$. This low porosity is similar to that of carbons derived from other biomass waste under lower carbonization temperature,[29] which may be due to the internal structure can not be completely destroyed under lower temperature. As the carbonization temperature increased from 700 to 900 ^oC, both the S_{BET} and V_{total} of the N-SACs increased obviously. The S_{BET} of N-SAC700 and N-SAC800 were determined to be 581, 1088 $m^2 g^{-1}$, while the pore volumes are 0.34 and 0.80 $cm^3 g^{-1}$, respectively. However, the S_{BET} and V_{total} of N-SAC900 decrease to 886.9 $m^2 g^{-1}$ and 0.62 $cm^3 g^{-1}$, respectively, which is probably due to the collapse of pores and enhanced orientation during the carbonization process.[15] As shown in Figure 4a, the N-SACx (x = 700-900) samples all exhibit typical Type IV adsorption-desorption isotherms with an obvious type-H4 hysteresis loop at p/p_0=0.4-0.9. The existence of type-H4 hysteresis loop is indicative of the presence of large mesopores embedded in the carbon matrix with interconnected channels of much smaller size. In contrast, the isotherm of N-SAC600 exhibits a typical type-I curve, indicating only a microporous structure.[27] Figure 4b depicts the pore size distribution curves determined by N_2 adsorption for these N-SACs based on Barrett-Joyner-Halenda (BJH) model, proving their multi-modal pore structures obviously. The co-existence of micro/meso/macro-scale pores in present work are believed to be ideal for supercapacitor, due to the actual energy storage occurring predominately in the appropriate micropores and small mesoporous, while the larger pores provide fast mass-transport of electrolytes to and from the micropores.[30]

The temperature can also influence the nitrogen content and chemical state in the carbons. Elemental and XPS analysis were employed to confirm the existence of nitrogen in the N-SACs.

The chemical compositions of the obtained carbon materials are shown in Table 1, it can be seen that all samples contain different amount of nitrogen species (1.51-5.13 wt %). The nitrogen atoms in the carbon matrix are considered to effectively improve the wettability and electrical conductivity of the carbon-based materials, which result in facilitate the accessibility of the electrolyte ions and enhance the capacitance performance.[31] In addition, the content of the nitrogen atoms in N-SACs decrease evidently with an increase of the carbonization temperature, which is due to the high carbonization temperature accelerates the decomposition of N-containing frameworks.[32] This means that obtained carbon materials with a high porosity and a high nitrogen content at the same time is difficult, therefore, with the appropriate carbonization temperature, it not only can make the precursor carbonized completely but also maintain high nitrogen contents in carbon skeleton. Besides, the oxygen contents evaluated from the XPS analysis are 5.94-7.44 wt.% in N-SACs. The attached oxygen atoms on the surface of the carbons are presumed to come from the moisture, atmospheric O_2 or CO_2 absorbed,[12] which also have a significant contribution to the capacitance performance because it is widely accepted that the O functionalities on carbons contribute to the pseudocapacitance through the quinone/hydroquinone redox pair.[11]

The high-resolution N 1s XPS spectra of N-SACs are shown in Figure 5. The high-resolution N 1s core level spectra can be deconvoluted by four peaks representing pyridinic N (N-6 at 398.0±0.2 eV), pyrrolic N (N-5 at 399.7±0.2 eV) quaternary N (N-Q at 400.8±0.2 eV) and oxidized N (N-X at 402.5±0.2 eV).[11] The relative contents of these different nitrogen species in N 1s are also summarized in Table 2. It is clear that with the increase of the temperature, the relative content of the N-5 and N-6 decreases, while the relative contents of the N-Q and N-X increase, suggesting a transformation of pyrrolic N and pyridinic N to quaternary N and oxidized N at a

higher temperature. As reported previously, N-6 and N-5 are assumed to be the main configurations contributing to the Faradaic reaction-based pseudocapacitance effect and thus increase the capacitance performance.[33] Moreover, the presence of N-G can enhance the electrical conductivity of carbon, which is beneficial for rate and cycling performances of supercapacitors.[15] It is worth noted that the relative content of the N-5 and N-6 in N-SAC700 up to 63.1%, which is benefit to increase the capacitance performance.

3.2 Electrochemical Behavior and Characterization

To investigate the electrochemical characteristics of the obtained carbon materials, cyclic voltammetry (CV), galvanostatic charge/discharge and electrochemical impedance measurements were employed to characterize the capacitive properties. The CV curves of all the carbon samples electrodes at a scan rate of 50 mV s^{-1} in the potential window of -1 to 0 V are shown in Figure 6a. The CV curves of N-SACs display a quasi-rectangular shape, showing a typical characteristic of double-layer capacitance behavior based on ionic adsorption and exchange. The good rectangular shape of N-SACx (x = 700-900) also imply that these electrodes have rapid charge and discharge feature. However, the CV curve of the N-SAC-600 electrode exhibits a small special shape which is apparently different from the EDLCs' typical rectangular shape, indicating the low capacitance due to the very low specific surface area and pore texture.[12] In the case of the galvanostatic charge/discharge curves of N-SACs sample, the voltage profiles (Figure. 6b) are non-linear, which suggests redox reactions associated to the presence of N-groups, more specifically to the presence of pyridinic-N, which is involved in proton exchange redox reactions.[34] Among the carbon samples, the N-SAC700 exhibits the largest CV curve area and longest discharge time, indicating the highest capacitance values. Moreover, N-SAC700 still presents a relatively rectangular CV

shape even at a fast sweeping rate of 100 mV s^{-1} (Figure 6c), implying efficient charge transfer and electrolyte diffusion within the N-SAC700 electrode.[35] Although the specific surface area of N-SAC800 (1088 m^2 g^{-1}) is higher than that of N-SAC700 (581.7 m^2 g^{-1}), the nitrogen content of N-SAC700 (4.06 wt.%) is more than that of N-SAC800 (2.9 wt.%), especially, the total content of the N-5 and N-6 in N-SAC700 up to 63.1%. The co-contribution of the high double-layer capacitance attributed to its high surface area and the additional pseudocapacitance mainly raised from the nitrogen-containing functional groups endows N-SAC700 with the highest capacitance values. This result demonstrates that a balanced specific surface area and nitrogen content is crucial for these nitrogen-doped porous carbons to obtain a superior electrochemical capacitive performance.[25]

The galvanostatic charge/discharge curves of N-SAC700 carbon sample at different current densities are presented in Figure 6d. It is clear that the shapes of the charge/discharge curves show isosceles triangular shapes even at the current densities as high as 10 A g^{-1}, indicating an excellent capacitive behavior and electrochemical reversibility. The specific capacitance values of N-SACs calculated from the charge/discharge curves at different current densities ranged from 0.5 to 10 A g^{-1} show that N-SAC700 exhibits the best specific capacitance (Fig. 6e). The max specific capacitance of N-SAC700 is 215 F g^{-1} obtained at the current density of 0.5 A g^{-1}, and higher than most previously reported carbon materials in the aqueous electrolytes (Table 3).[36-43] Furthermore, the N-SAC700 shows a capacitance of 130 F g^{-1} even at a high current density of 10 A g^{-1} (preserves 70% of its capacitance delivered at 1 A g^{-1}), which is a attractive value for supercapacitors and indicating favorable capacitance retention. This result suggests that N-SAC700 has a good rate capability, which is very important for the electrode materials of

supercapacitors to provide high power density. The excellent performance of such a porous carbon material may be attributed to the combination of wrinkled structure with abundant of meso/microporous structure and high nitrogen-doped content, which probably enhance the kinetics of ion and electron transport in electrodes and at the electrode/electrolyte interface.

To understand the excellent performance of N-SAC700, the facilitated ion and electron transport behavior of N-SACs materials were investigated using electrochemical impedance spectroscopy (EIS) under the open circuit potential. Figure 6f shows the Nyquist plots obtained at a frequency range from 0.1 to 10^5 Hz, with an expanded view of the high frequency region in the inset. At high frequency region, the intercept of plot with real axis represents the equivalent series resistance (Rs), which is a combination of the ionic resistance of the electrolyte, intrinsic resistance of the active materials, and contact resistance with the current collector.[29] It can be observed that the impedance plots of the N-SACs displays a small approximate semicircular at high frequenciy region and the Rs values are 3.77, 3.75, 4.52, 4.39 Ω for N-SAC600, N-SAC700 N-SAC800, N-SAC900, respectively, which indicates that the N-SAC700 electrode has a low resistance with a good ion response at high frequency ranges.[44] From the magnified data in the medium frequencies, a transition line with a slope of 45^o between the semicircle and the migration of the electrolyte was observed, caused by diffusion impedance and known as the Warburg impedance. The Warburg resistance section was very short, indicating that the electrolyte ions had efficient access to the electrode surface.[18] In the low frequency region, a straight line approaching 90^o is obtained, representing an ideal capacitive behavior of the electrode.[35] The EIS results further demonstrate that the N-SAC700 porous carbon material has the good electrical conductivity and the ability of rapid electron and ion transport.

The cycling stability is also a crucial parameter for supercapacitors electrode materials. To investigate the cycling stability, the galvanostatic charge/discharge cycling of the N-SAC700 was performed at a current density of 5 A g^{-1} (Figure 7). After 5000 cycles, the capacity decay is only 8% compared with the starting value, indicating the good cycling stability, which may be due to the surface functional groups strongly bonding with the carbon and keeping stable during cycling, and the faradaic reactions based on the surface functional groups being fully reversible.[12] This result makes it a promising candidate for long-term energy storage devices.

To further evaluate the capacitive performance and simulate the actual device behaviour of the N-SAC700 electrode, a symmetric supercapacitor based on the same two N-SAC700 electrodes was fabricated. Compared with KOH and H_2SO_4 electrolytes, Na_2SO_4 electrolyte possesses a higher operation voltage due to its low H^+ and OH^- concentration, oxygenated surface functionalities on carbon surface that result in high over-potential for dihydrogen evolution.[16] Therefore, the N-SAC700 symmetric supercapacitor was assembled with 0.5 M Na_2SO_4 aqueous electrolyte. Figure 8a exhibits CV curves of N-SAC700//N-SAC700 symmetric cell at different potential windows from 1.0 to 2.0 V at a scan rate of 20 mV s^{-1}. It can be seen that the as-fabricated symmetrical cell can be reversibly cycled within the voltage window of 0-1.8 V. However, when the operating voltage increases to 2.0 V, the current increases sharply in high voltage since the electrolyte could be decomposed to hydrogen and/or oxygen.[24] Therefore, the wide potential window of 1.8 V is chosen to further estimate the electrochemical performance of the N-SAC700//N-SAC700 symmetric cell.

The CV curves of as-assembled N-SAC700//N-SAC700 symmetric cell (Figure 8b) show a quasi-rectangular shape even at a high scan rate of 100 mV s^{-1}, indicating an ideal capacitive

behavior owing to the porous structure ensuring effective accessibility of electrolyte ions at high charge/discharge rates for the as-assembled symmetric cell. Galvanostatic charge/discharge curves of the symmetric cell at different current densities from 0.25 to 5 A g^{-1} (Figure 8c) exhibit perfect highly linear and symmetrical, confirming that the as-fabricated N-SAC700//N-SAC700 symmetric supercapacitor has a good electrochemical reversibility.

In order to further determine the electrochemical performance of the N-SAC700 carbon materials, Ragone plot (specific energy *vs* specific power) of N-SAC700//N-SAC700 symmetric cell was calculated as shown in Figure 8d. The N-SAC700//N-SAC700 cell exhibits the highest energy density is 9.95 Wh Kg^{-1} at a power density of 236 W Kg^{-1} and even remained 3.87 Wh Kg^{-1} at a power density of 4644 W Kg^{-1}, which means that less energy can be released at higher power output. Even though the energy density of N-SAC700 may be undesirable, it is still apparently superior to the recently reported porous carbons.[39,45-48,41] Hence, the biowaste soybean curd residue derived porous carbons are still promising electrode materials for supercapacitors.

4 Conclusions

A high-performance porous carbon material for supercapacitors has been obtained by one-step carbonization of the nitrogen-enriched precursor (SCR). The co-contribution of the high double-layer capacitance attributed to its high surface area and the additional pseudocapacitance mainly raised from the nitrogen-containing functional groups endows N-SAC700. Moreover, the assembled N-SAC700//N-SAC700 supercapacitor device demonstrates a highest energy density of 9.95 Wh kg^{-1} at a power density of 236 W Kg^{-1}, which is higher than that of other previously reported carbon-based symmetric supercapacitors. Considering that large amount of biowaste soybean curd residue are generated in the process of soybean products, the carbon material can be

produced at low cost and large-scalable for the supercapacitor industry. Therefore, the strategy developed in this work could open up a novel and eco-friendly route for preparation of high performance supercapacitor electrode materials from renewable biomass waste.

Acknowledgements

We thank the Science and Technology program of Gansu Province (no. 1308RJZA295, 1308RJZA265), the National Science Foundation of China (no. 21164009, 21174114), the program for Changjiang Scholars and Innovative Research Team in University (IRT1177), Lanzhou City University (LZCU-BS2013-11), Key Laboratory of Eco-Environment-Related Polymer Materials of Ministry of Education, and Key Laboratory of Polymer Materials of Gansu Province.

References

1. S. Chu and A. Majumdar, *Nature*, 2012, **488**(7411), 294-303.

2. B. Dunn, H. Kamath and J. M. Tarascon, *Science*, 2011, **234**, 928-35.

3. X. Wang, B. Liu, R. Liu, Q. Wang, X. Hou, D. Chen and G. Shen, *Angew. Chem. Int. Edit.*, 2014, **126**(7), 1880-1884.

4. H. Chen, S. Zeng, M. Chen, Y. Zhang and Q. Li, *Carbon*, 2015, **92**, 271-296.

5. G. Sun, X. Zhang, R. Lin, J. Yang, H. Zhang and P. Chen, *Angew. Chem. Int. Edit.*, 2015, **127**(15), 4734-4739.

6. M. Sevilla and A. B. Fuertes, *ACS nano*, 2014, **8**(5), 5069-5078.

7. S. Faraji and F. N. Ani, *Renew. Sust. Energ. Rev.*, 2015, **42**, 823-834.

8. H. Jeong, H. J. Kim, Y. J. Lee, J. Y. Hwang, O. K. Park, J. H. Wee and J. K. Lee, *Mater. Lett.*, 2015, **145**, 273-278.

9. J. Han, G. Xu, B. Ding, J. Pan, H. Dou and D. R. MacFarlane, *J. Mater. Chem. A.*, 2014, **2**(15), 5352-5357.

10. S. L. Candelaria, B. B. Garcia, D. Liu and G. Cao, *J. Mater. Chem.*, 2012, **22** (19) 9884-9889.

11. Z. Li, Z. Xu, H. Wang, J. Ding, B. Zahiri, C. M. Holt and D. Mitlin, *Energ. Environ. Sci.*, 2014, **7**(5), 1708-1718.

12. M. Zhou, F. Pu, Z. Wang and Guan, S. *Carbon*, 2014, **68**, 185-194.

13. L. Wan, J. Wang, L. Xie, Y. Sun and K. Li, *ACS appl. Mater. inter.*, 2014, **6**(17), 15583-15596.

14. L. F. Chen, Z. H. Huang, H. W. Liang, W. T. Yao, Z. Y. Yu and S. H. Yu, *Energ. Environ. Sci.*, 2013, **6**(11), 3331-3338.

15. W. Qian, F. Sun, Y. Xu, L. Qiu, C. Liu, S. Wang and F. Yan, *Energ. Environ. Sci.*, 2014, **7**(1), 379-386.

16. C. Long, X. Chen, L. Jiang, L. Zhi and Z. Fan, *Nano Energy*, 2015, **12**, 141-151.

17. W. H. Qu, Y. Y. Xu, A. H. Lu, X. Q. Zhang and W. C. Li, *Bioresource technol.*, 2015, **189**, 285-291.

18. Y. S. Yun, M. H. Park, S. J. Hong, M. E. Lee, Y. W. Park and H. J. Jin, *ACS appl. Mater.inter.*, 2015, **7**(6), 3684-3690.

19. D. Bhattacharjya and J. S. Yu, *J. Power Sources*, 2014, **262**, 224-231.

20 S. Li, L. Wang, C. Song, X. Hu, H. Sun, Y. Yang and Z. Zhang, *J. Taiwan Inst. Chem. E.*, 2014, **45**(1), 6-11.

21. D. Zhu, H. Sun, S. Li, X. Hu, X. Yuan, C. Han and Z. Zhang, *International Journal of Biology*, 2014, **7** (1), 82-92.

22. M. Shi, Y. Yang, Q. Wang, Y. Zhang, Y. Wang and Z. Zhang, *Int. J. Food Sci.Tech.*, 2012, **47**,

1215-1221.

23. J. J. Almaraz, X. Zhou, F. Mabood, C. Madramootoo, P. Rochette, B. L. Ma and D. L. Smith,. *Soil Till. Res.,* 2009, **104**(1), 134-139.

24. H. Peng, G. Ma, K. Sun, J. Mu, Z. Zhang and Z. Lei, *ACS appl. Mater. Inter.*, 2014, **6**(23), 20795-20803.

25. L. Zhu, Q. Gao, Y. Tan, W. Tian, J. Xu, K. Yang and C. Yang, *Micropor. Mesopor. Mater.*, 2015, **210**, 1-9.

26. Q. Zhao, X. Wang, C. Wu, J. Liu, H. Wang, J. Gao and Y. Zhang, *J. Power Sources*, 2014, **254**, 10-17.

27. T. Wei, X. Wei, Y. Gao and H. Li, *Electrochim. Acta*, 2015, **169**, 186-194.

28. Y. Tan, C. Xu, G. Chen, Z. Liu, M. Ma, Q. Xie and S.Yao, *ACS appl. Mater. Inter.*, 2013, **5**(6), 2241-2248.

29. Y. Fan, X. Yang, B. Zhu, P. F. Liu and H. T. Lu, *J. Power Sources*, 2014, **268**, 584-590.

30. X. Y. Chen, C. Chen, Z. J. Zhang, D. H. Xie, X. Deng and J. W. Liu, *J. Power Sources*, 2013, **230**, 50-58.

31. J. Jiang, L. Bao, Y. Qiang, Y. Xiong, J. Chen, S. Guan and J. Chen, *Electrochim. Acta*, 2015, **158**, 229-236.

32. J. Wei, D. Zhou, Z. Sun, Y. Deng, Y. Xia and D. Zhao, *Adv. Funct. Mater.*, 2013, **23**(18), 2322-2328.

33. D. Usachov, O. Vilkov, A. Gruneis, D. Haberer, A. Fedorov, V. K. Adamchuk and Vyalikh, D. V, *Nano lett.*, 2011, **11**(12), 5401-5407.

34. G. A. Ferrero, A. B. Fuertes and M. Sevilla, *Electrochim. Acta*, 2015, **168**, 320-329.

35. L. Sun, C. Tian, M. Li, X. Meng, L. Wang, R. Wang and H. Fu, *J. Mater. Chem. A*, 2013, **1**(21), 6462-6470.

36. Y. Guo, J. Qi, Y. Jiang, S. Yang and Z. Wang, *Mater. Chem. Phys.*, 2003, **80**, 704-709.

37 F. C. Wu, R. L. Tseng, C. C. Hu and C.C.Wang, *J. Power Sources*, 2004, **138**, 351-359.

38. V. Subramanian, C. Luo, A. M. Stephan, K. S. Nahm, S. Thomas and B. Wei, *J. Phys. Chem. C.*, 2007, **111**, 7527-7531.

39. H. Zhu, X. Wang, F. Yang and X. Yang, *Adv. Mater.*, 2011, **23**(24), 2745-2748.

40. M. P. Bichat, E. Raymundo-Piñero and F. Béguin, *Carbon*, 2010, **48**(15), 4351-4361.

41. E. Raymundo-Piñero, F. Leroux and F. Béguin, *Adv. Mater.*, 2006, **18**, 1877-1882.

42. J. Ma, W. Huang, K. Chen, D. Xue and S. Komarneni, *Nanosci. Nanotech. Lett.*, 2014, **6**(11), 997-1000.

43. F.C. Wu, R. L. Tseng, C. C. Hu and C. C. Wang, *J. Power Sources*, 2005,**144**, 302-309.

44. P. Yu, Y. Li, X. Yu, X. Zhao, L. Wu and Q. Zhang, *Langmuir*, 2013, **29**(38), 12051-12058.

45. X. Fan, C. Yu, J. Yang, Z. Ling and J. Qiu, *Carbon*, 2014, **70**, 130-141.

46. X. Li, W. Xing, S. Zhuo, J. Zhou, F. Li, S. Z. Qiao and G. Q. Lu,. *Bioresource technol.*, 2011, **102**(2), 1118-1123.

47. X. He, R. Li, J. Qiu, K. Xie, P. Ling, M. Yu and M. Zheng, *Carbon*, 2012, **50**(13), 4911-4921.

48. Z. Lei, N. Christov, L. L. Zhang and X. S. Zhao, *J. Mater. Chem.*, 2011, **21**(7), 2274-2281.

Figure captions:

Table 1 Elemental analysis, BET surface area and pore structure characterization parameters of N-SACs from different carbonization temperatures.

Table 2 Relative content of nitrogen species obtained by fitting the N1s core level XPS spectra.

Table 3 Comparison of electrochemical performance of activated carbons from biomass precursors

Scheme 1. The preparation process of N-SACs.

Figure 1 FE-SEM for the samples: (a) N-SAC600; (b) N-SAC700; (C) N-SAC800; (d) N-SAC900.

Figure 2 TEM images of the N-SAC700 under different magnifications.

Figure 3 (a) XRD pattern and (b) Raman spectra of N-SAC700 sample.

Figure 4 (a) Nitrogen adsorption-desorption isotherms and (b) pore size distribution curves of N-SACs from different carbonization temperatures.

Figure 5 XPS spectra of samples: (a) N-SAC600; (b) N-SAC700; (C) N-SAC800; (d) N-SAC900.

Figure 6 (a) CV curves of N-SACs electrodes at a scan rate of 50 mV s^{-1} in 2 M KOH solution; (b) Galvanostatic charge/discharge curves of N-SACs electrode at a current density of 0.5 A g^{-1}; (c) CV curves of N-SAC700 electrode at different scan rates; (d) Galvanostatic charge/discharge curves of N-SAC700 electrode at various current densities; (e) Discharge capacitances of N-SACs electrode at various current densities; (f) Nyquist plots of N-SACs electrode in three-electrode system.

Figure 7 Cycling stability of N-SAC700 in three-electrode system.

Figure 8 (a) CV curves of the N-SAC700 symmetric two-electrode cell at different voltage windows in 0.5 M Na_2SO_4 aqueous electrolyte; (b) CV curves of the N-SAC700 symmetric cell at various scan rates; (c) Galvanostatic charge/discharge curves of N-SAC700//N-SAC700 symmetric cell at various current densities; (d) Ragone plot of the N-SAC700//N-SAC700 symmetric cell and other previously reported carbon-based symmetric supercapacitors.

Table 1

Samples	Element content analysis				S_{BET} [b)] ($m^2 g^{-1}$)	V_{total} [c)] ($cm^3 g^{-1}$)	APD [d)] (nm)
	C%	N%	H%	O% [a)]			
N-BAC600	73.76	5.13	1.75	7.44	9.78	0.016	6.52
N-BAC700	72.33	4.06	1.99	6.43	581.74	0.34	2.37
N-BAC800	72.93	2.90	1.65	6.68	1088.11	0.80	2.95
N-BAC900	82.57	1.51	1.34	5.94	886.99	0.62	2.79

a) Weight percent of oxygen element obtained from XPS analysis

b) Specific surface area from multiple BET method.

c) Total pore volume at P/P_0=0.99.

d) Adsorption average pore diameter.

Table 2

Samples	N %[a)]	Nitrogen species (%)			
		N-Q	N-5	N-6	N-X
N-BAC600	5.03	35.8	24.3	27.3	12.6
N-BAC700	3.95	28.4	39.4	23.7	8.5
N-BAC800	2.59	38.7	26.2	21.6	13.4
N-BAC900	1.89	36.1	27.9	19.2	16.8

a) Weight percent of nitrogen elements obtained from XPS analysis

Table 3

Carbon precursor	Activation Method	Gravimetric Capacitance ($F\ g^{-1}$)	Capacitance measurement at	Electrolyte	Ref.
Rice husk	NaOH	210	0.2 mA g^{-1}	3 M KCl	36
Firwood	H_2O	140	25 mV s^{-1}	0.5 M H_2SO_4	37
Banana fibers	$ZnCl_2$	74	0.5 A g^{-1}	1 M Na_2SO_4	38
Auricularia	Thermal	196	5 mVs^{-1}	6M KOH	39
Seaweed	Thermal	244	2 mVs^{-1}	6M KOH	40
Seaweed biopolymer	Not used	198	-	1M H_2SO_4	41
Banana peels	KOH	158	1 A g^{-1}	2 M KOH	42
Pistachio shell	KOH	120	10 mV s^{-1}	0.5M H_2SO_4	43
Soybean curd residue	Not used	215	0.5 A g^{-1}	2M KOH	This work

Scheme 1

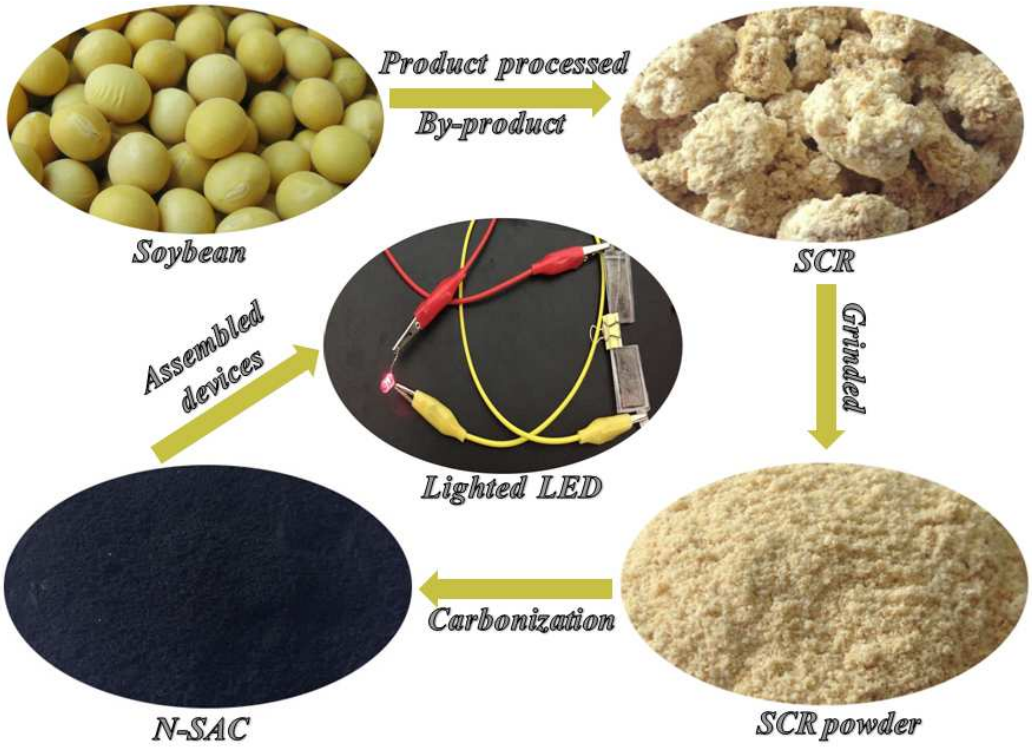

Figure 1

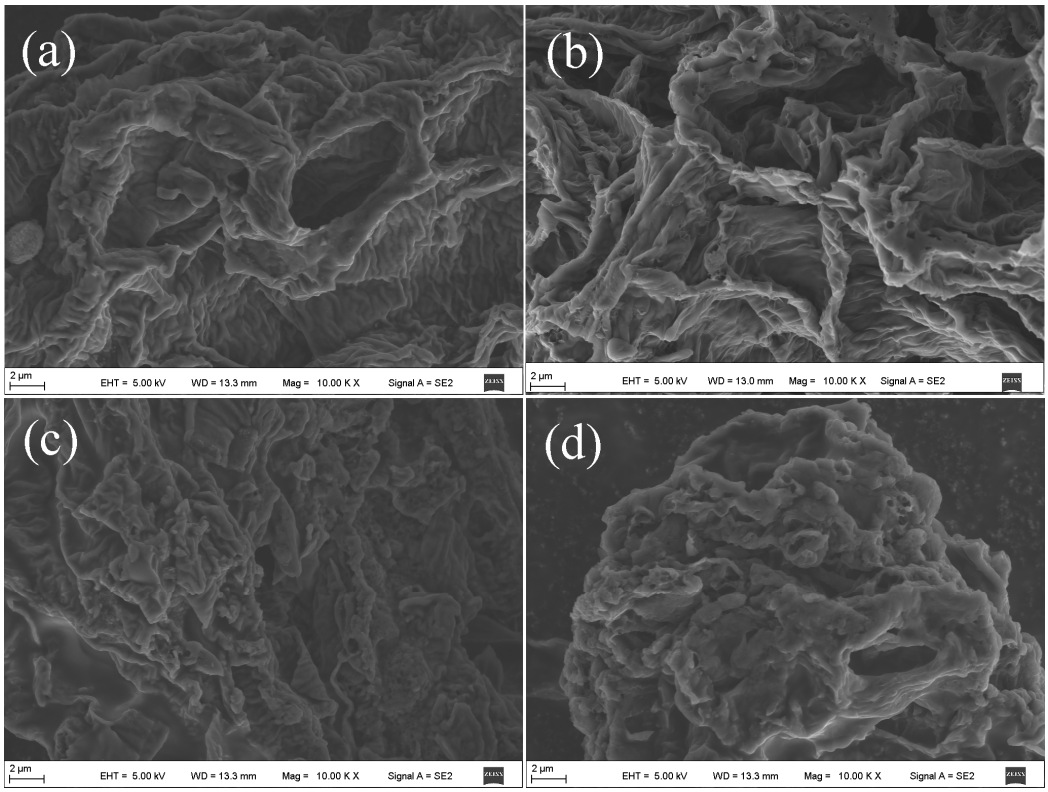

Figure 2

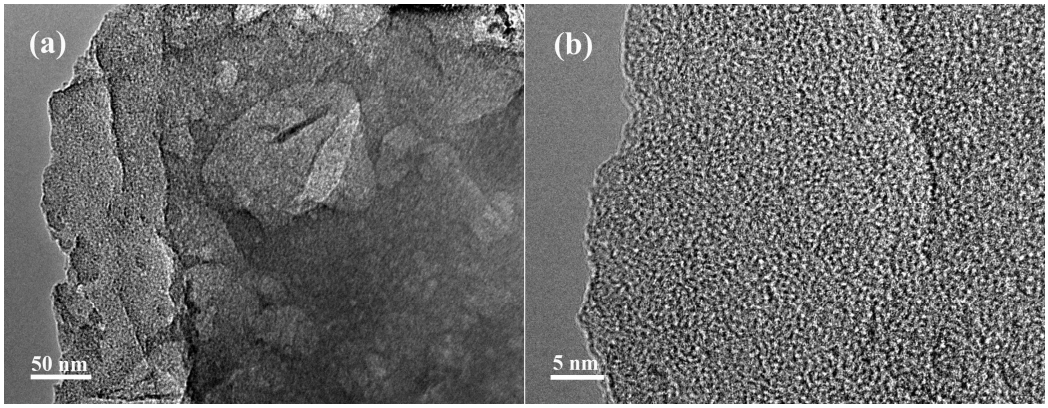

Figure 3

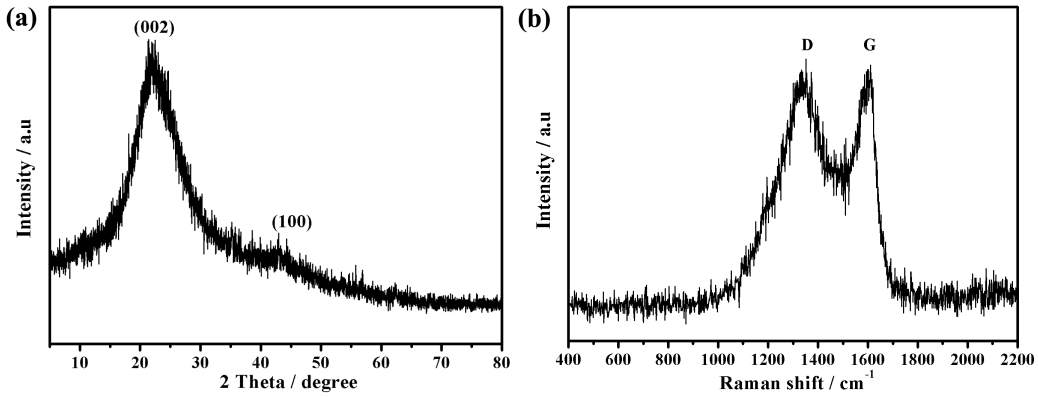

Figure 4

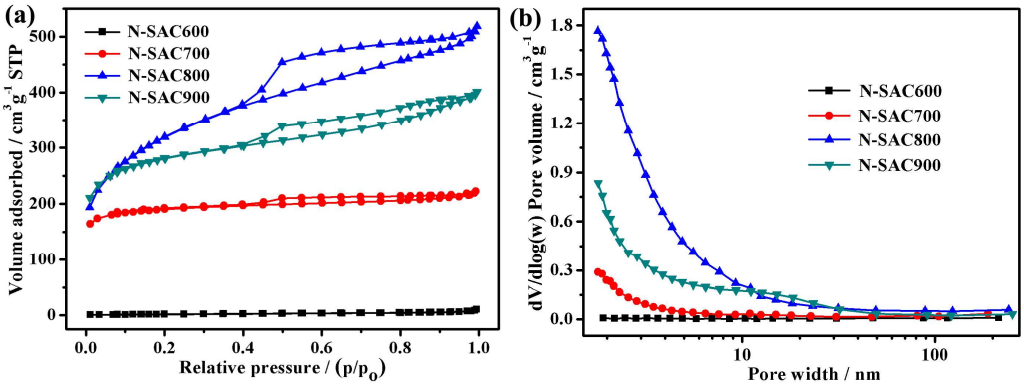

Figure 5

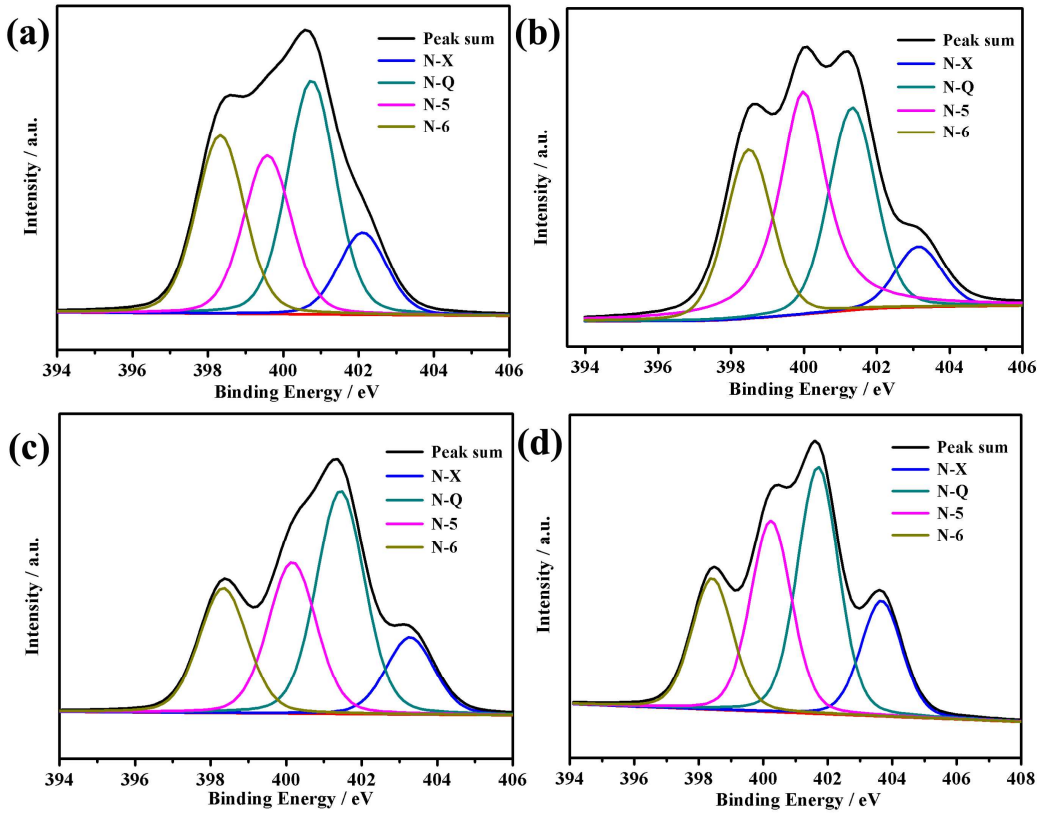

Figure 6

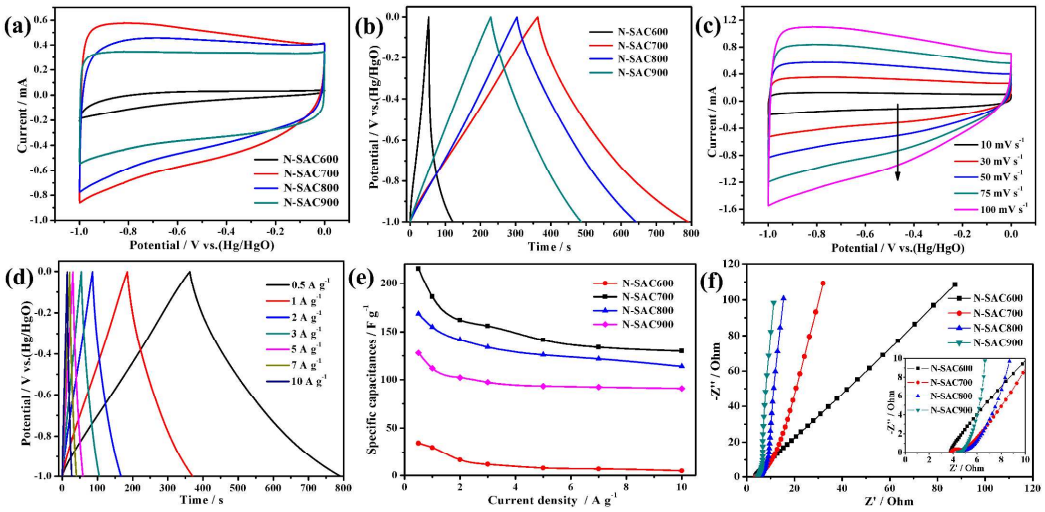

Figure 7

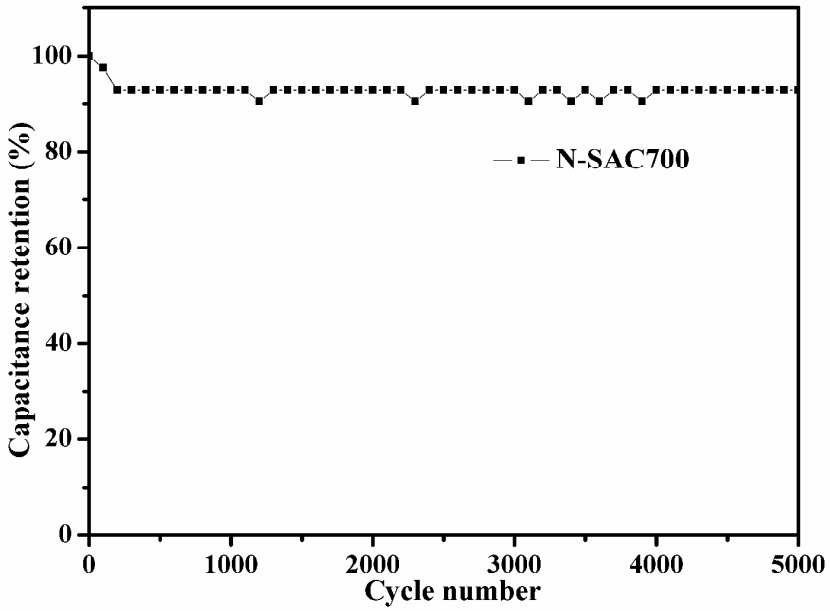

Figure 8